ORIGINAL PAPER

Nucleation theory applied to the development of contrasting garnet crystal densities

Frank S. Spear[1] · Oliver M. Wolfe[1]

Abstract

Rocks that contain numerous small garnets (high crystal density or HiCD) and few large garnets (low crystal density or LoCD) have been examined from three localities in New England to constrain the degree of overstepping for garnet nucleation. Garnet crystal densities have been measured in nine samples and range from a few crystals/cm^3 to over 100×10^6 crystals/cm^3. Quartz-in-garnet (QuiG) barometry reveals that the quartz inclusion isomekes in HiCD samples are within error the same pressure as quartz inclusion isomekes in LoCD samples, suggesting similar P–T conditions of nucleation. Temperature of nucleation is more difficult to constrain but several lines of reasoning suggest that both HiCD and LoCD samples nucleated garnet at similar P–T conditions, which are, in all cases, significantly above the calculated equilibrium garnet-in reaction. Affinities for garnet nucleation calculated using the Maximum Driving Force (MDF or parallel tangent) approach range from 0.15 to 0.5 kJ/mol-O in the LoCD samples to 1.4–4.3 J/mol-O in the HiCD samples using the SPaC thermodynamic dataset and 0.65–1.8 kJ/mol-O in the LoCD samples to 3.0–6.1 J/mol-O in the HiCD samples using the HP11 thermodynamic dataset. Application of classical nucleation theory permits constraining the surface energy at the time of nucleation to approximately 0.022–0.045 J/m^2 depending on the thermodynamic dataset used and places limits on the pre-exponential constant in the rate equation. The question of why proximal samples should accumulate such different amounts of affinity before garnet nucleates is unanswered, but it is clear that some factor other than just the amount of chemical affinity must be important.

Keywords Garnet · Nucleation · Coticule · QuiG barometry · Crystal density · Affinity

Introduction

Rocks with numerous small garnets (high crystal densities or HiCDs) are often found associated with rocks with few large garnets (low crystal densities or LoCDs). Some of these HiCD rocks are coticules, which is an uncommon metamorphic rock characterized by moderately high bulk MnO contents and numerous small (5–200 μm diameter) garnets (e.g., Thomson 2001; Willner et al. 2001; Herbosch et al. 2016) but others are quartzites, metavolcanics or metapelites.

The presence of numerous tiny garnets in HiCD samples can readily be explained by noting that the rate of nucleation

✉ Frank S. Spear
spearf@rpi.edu

1 Department of Earth and Environmental Sciences, Rensselaer Polytechnic Institute, 110 8th Street, Troy, NY 12180, USA

must have greatly exceeded rate of garnet growth. However, and most significantly, these HiCD rocks are often found in sequences that also contain more normal quartzites, metapelites and metavolcanics with average sized (1–5 mm diameter) garnets. But this raises the question as to why the nucleation rate in the HiCD rocks was so much more rapid than the growth rate in these rocks, whereas the growth rate in nearby LoCD rocks was considerably more rapid relative to the nucleation rate.

Nucleation of a new phase such as garnet requires sufficient chemical affinity, generated by overstepping of the equilibrium phase-in reaction, to overcome the nucleation barrier. The purpose of this paper is to attempt to place some constraints on the energetics of garnet nucleation and growth by comparison of the degree of overstepping evidenced by HiCD and nearby LoCD rocks. In order to do so, it is necessary to first constrain P–T conditions of garnet nucleation to determine the amount of overstepping in each. This contribution utilizes a combination of approaches for this purpose including inclusion barometry (quartz-in-garnet or

QuiG), classical and trace element thermo-barometry, and thermodynamic calculations.

The samples chosen for this study are from three localities in New England (Table 1). Locality 1 is in the Orfordville belt in West–Central New Hampshire and East–Central Vermont. The metamorphic grade is in the staurolite–kyanite zone with peak pressure–temperature (P–T) conditions around 600 °C, 0.5–0.6 GPa (Spear and Rumble 1986; Spear and Wolfe 2020). Sample 79-149d (the LoCD sample) is a garnet–staurolite–kyanite schist and garnet was interpreted by Spear and Rumble (1986) to have grown along a clockwise P–T path assuming equilibrium growth but Spear and Wolfe (2020) concluded based on QuiG barometry that garnet growth was more likely isothermal and isobaric. The HiCD sample from this locality (77-51b) is an amphibolite located 1.3 km along strike from sample 79-149d and no previous studies have been made of this sample.

Locality 2 is located in western Massachusetts along US Rt. 9 (Table 1). Sample OW-17 m (the LoCD sample) is a garnet–chlorite schist that contains several large (ca. 1 cm diameter) garnets that were described in detail by Wolfe and Spear (2020). Sample OW-17b is a quartzite from the same outcrop and has not been previously studied.

Locality 3 is located in northern New Hampshire along the Bronson Hill anticlinorium. The HiCD samples 79-112c and 79-114c are located within 0.8 km of the LoCD sample 79-115b,c and the HiCD sample 79-103i is located approximately 6.75 km to the north. All samples are mapped as belonging to the Smalls Falls Formation and are characterized as quartzite, phyllite and schist (Table 1). No previous petrology has been done on these samples.

Selected photomicrographs for each LoCD sample are included in the supplemental materials (Online Resource 1).

Methods

Analytical methods

Bulk rock chemical analyses were determined by scanning polished thin sections over the compositional layer of interest and collecting a single chemical analysis using an energy dispersive detector. The samples studied display compositional layering, even on the thin-section scale, and the above approach was adopted so that the bulk composition of only the layer under study would be analyzed. For the HiCD samples, the area scanned was large relative to the grain size (e.g., 25–30 mm^2 area with average grain area less than 0.005 mm^2 = radius < 0.1 mm). For the LoCD samples, the area scanned was typically the entire polished thin section (e.g., ~ 1000 mm^2). Standards used were natural and synthetic silicates and oxides. Quantitative chemical analyses of phases were collected using wavelength dispersive spectrometers using the same standard materials. All analyses were done using the Cameca SX-100 at Rensselaer Polytechnic Institute (see Wolfe and Spear 2018, for additional details of the methodology).

Nucleation rate

Calculation of nucleation rate from a natural sample requires first measuring the crystal density, which has been done by both point counting with the optical microscope and image analysis. Inasmuch as crystal densities were determined on 2-D images (BSE images and X-ray maps), it is not possible to determine the 3-D density without making assumptions about the crystal size distribution. Calculations were done in two ways: (a) assuming that all crystals had the diameter of the largest crystal in the sample, which yielded the

Table 1 Sample locations, formations, rock types, and mineralogy

Sample	Type[a]	Latitude	Longitude	Quadrangle	Formation	Rock type	Minerals present
Locality 1							
77-51b	HiCD	43.78380	− 72.22825	Mt. Cube 15' VT	Post Pond Volcs	Amphibolite	Qtz Plg Grt Hbl Bt
79-149d	LoCD	43.77335	− 72.23648	Mt. Cube 15' VT	Littleton	Schist	Qtz Plg Ms Grt Bt St Ky
Locality 2							
OW-17b	HiCD	42.48647	− 72.94163	Worthington 7.5' MA	Hawley	Quartzite	Qtz Plg Grt Bt Ilm Ank Ap
OW-17 m	LoCD	42.48647	− 72.94163	Worthington 7.5' MA	Hawley	Chlorite-garnet schist	Qtz Plg Grt Bt Chl Ilm Ep Ap
Locality 3							
79-103i	HiCD	44.81092	− 71.23758	Errol 15' NH	Smalls Falls	Quartzite	Qtz Grt Act
79-112c	HiCD	44.74725	− 71.24769	Percy 15' NH	Smalls Falls	Quartzite	Qtz Plg Grt Bt Chl Ap
79-114c	HiCD	44.74869	− 71.23807	Percy 15' NH	Smalls Falls	Phyllite	Qtz Plg Grt Bt Ap Ttn
79-115b	LoCD	44.74873	− 71.23632	Percy 15' NH	Smalls Falls	Schist	Qtz Plg Grt Bt Chl Ilm Ap
79-115c	LoCD	44.74873	− 71.23632	Percy 15' NH	Smalls Falls	Schist	Qtz Plg Grt Bt St Ilm Ap Ksp

[a]"Type" refers to HiCD (high crystal density) and LoCD (low crystal density)

lowest value for crystal density, or (b) using an estimate of the average crystal diameter. With either of these assumptions, the 3-D crystal density is simply calculated as 3-D density = 2-D density/crystal diameter, assuming the crystals are perfect spheres. For example, a sample composed of crystal spheres with diameters of 0.1 cm and a 2-D crystal density of 100 crystals/cm^2 would have a 3-D crystal density of 1000 crystals/cm^3. Results from both approaches are listed in Table 2. Inasmuch as the actual average crystal size is certainly smaller than the largest crystal observed and may be smaller than the estimated average size, the calculated nucleation densities are minimum estimates. The above method was chosen over X-ray tomography (e.g., Kelly et al. 2013) because the HiCD samples contain crystals with diameters of only a few μm, which would not be resolved with current X-ray tomography technology. Uncertainties in the measured crystal densities can be inferred by comparing the range of values for an individual sample. For all HiCD samples except OW-17b, the range of crystal densities measured using different methods varies within a factor of 2. The two methods listed for sample OW-17b differ by over an order of magnitude. However, uncertainties of even an order of magnitude in the measured crystal densities do not impact the results of this study because of the exponential dependence of affinity on nucleation rate, as discussed below.

Nucleation rates were inferred by estimating the time over which the nucleation has occurred. This time frame could, in principle, be ascertained by dating numerous garnet cores and examining the spread of ages, but the temporal resolution of existing geo-chronologic methods is insufficient for this task. The approach taken here is to assume that nucleation occurred over the same time interval in each sample. The implications of this assumption on the conclusions will be discussed in a later section.

Thermo-barometry

The pressure–temperature (P–T) conditions of garnet nucleation were estimated by integrating several approaches. Isomekes from quartz-in-garnet (QuiG) barometry were determined from Raman spectroscopy and it was assumed that garnet formation occurred along this line in P–T space. The 464 cm^{-1} band in quartz was used exclusively, as it has been shown experimentally to faithfully recover pressures of entrapment up to 2.5 GPa (Thomas and Spear 2018). The thermoelastic model of Guiraud and Powell (2006) with modifications by Angel et al. (2017) and constants constrained by the experimental data were used to calculate isomekes.

The temperature of garnet nucleation is difficult to constrain because appropriate geo-thermometers in the HiCD garnets are generally not available. In several LoCD samples, quartz inclusions were sufficiently large to enable the measurement of Ti concentrations, which provide a lower limit to the temperature of garnet growth (calibration of Thomas et al. 2010). Peak conditions were determined from garnet rim compositions using conventional thermo-barometry (garnet–biotite and garnet–hornblende Fe–Mg exchange using the calibration of Hodges and Spear 1982, and Graham and Powell, 1984, respectively) and calculated mineral assemblage diagrams (MADs or pseudo-sections) with Program Gibbs using the SPaC thermodynamic dataset of Spear and Pyle (2010), and the datasets of Holland and Powell (1998, 2011: HP98 with ds5.5 and HP11 with ds6.2, respectively, with activity models of White et al. (2014a, b—ds6.2).

Table 2 Garnet crystal densities

Sample	Type	Largest crystal diameter (μm)	Image analysis[a] Crystals/cm^3	Optical point count[b] Crystals/cm^3
Locality 1				
77-51b	HiCD	70	4.6×10^6	$2.4–4.6 \times 10^6$
79-149d	LoCD	2600	–	7
Locality 2				
OW-17b	HiCD	100	0.5×10^6	$3.2–8.0 \times 10^6$
OW-17 m	LoCD	5500	–	2.7
Locality 3				
79-103i	HiCD	25	190×10^6	$120–250 \times 10^6$
79-112c	HiCD	106	$0.3–0.9 \times 10^6$	$0.8–1.6 \times 10^6$
79-114c	HiCD	71	1.1×10^6	$3–6 \times 10^6$
79-115b	LoCD	1480	–	30
79-115c	LoCD	1020	–	21

[a]BSE and X-ray map images. Assumes largest crystal diameter

[b]Optical microscope. Assumes average crystal diameter

Affinity

Evaluating the affinity at the point of nucleation requires determination of the P–T conditions at which garnet nucleated and calculating the degree of overstepping relative to the equilibrium garnet formation P–T conditions. The equilibrium garnet-in conditions and affinities were calculated for all samples using the SPaC, HP98 (ds5.5) and HP11 (ds6.2) datasets. The magnitude of the affinity is calculated by comparing the Gibbs free energy of the nascent nucleus with that of the matrix from which the nucleus forms using the so-called maximum driving force (MDF) or parallel tangent approach (Fig. 1; Thompson and Spaepen 1983; Hillert 2008; Pattison et al. 2011; Gaidies et al. 2011; Spear et al. 2014). A generalized derivation of the MDF equations is presented in Spear and Wolfe (2019) and involves solving the system of equations that define the tangent plane for the matrix assemblage and the parallel tangent plane for garnet. Calculated in this way, the affinity is the maximum change in ΔG for the formation of a new nucleus, as discussed in detail by Pattison et al. (2011), Gaidies et al. (2011), Spear et al. (2014), Spear (2017), Spear and Wolfe (2019), and Castro and Spear (2016). Calculations of the garnet-in reaction and affinities associated with overstepping using the HP98 and HP11 datasets are included in the supplemental material (Online Resources 2 and 3).

All calculations were done using Program Gibbs and a detailed description of the operation and capabilities of Program Gibbs is included in the supplemental materials (Online Resource 4).

Results

Textural and mineralogical characteristics of the samples are displayed in Figs. 2, 3, 4, 5, 6, 7. Garnet crystals in HiCD samples range in diameter from under 10 μm to a couple of hundred μm. Given the generally small size of HiCD garnet, they typically display a surprising amount of chemical zoning in Mn and Ca. For example, sample 71-51b (Fig. 2) has rims low in Mn and enriched in Ca, sample 79-103i (Fig. 3) has some crystals with low Ca cores and others with high Ca cores, sample 79-112c (Fig. 4) shows Mn enriched rims and a high-Ca annulus, and sample OW-17b (Fig. 7) has crystals with high Mn cores, low Mn near-rim, and higher Mn rims whereas Ca is zoned in the opposite manner (Fig. 7d). LoCD garnet from the 3 localities all display typical Mn and Ca-enriched cores (e.g., Fig. 6). Chemical zoning in garnet from samples 79-149d and OW-17 m is similar to that in the other LoCD samples as was reported by Spear and Rumble (1986) and Wolfe and Spear (2018).

Measured crystal densities are presented in Table 2. Values range from 3 crystals/cm^3 (sample OW-17 m) up to 250 million crystals/cm^3 (sample 79-103i). The extremely high crystal density of sample 79-103i can be better understood by considering that the average size of the crystals is quite small (Fig. 3). The largest crystal observed has a diameter of around 25 μm (Fig. 3b) but the average crystal size is considerably smaller. As a reference, a cube with an area of 1 cm^3 could contain over 10^9 spheres of 10 μm diameter. Even if the modal amount of the spheres is only 10%, this still results in a crystal density of over 100 million per cm^3.

Both positive and negative Raman shifts (relative to matrix quartz) were observed in quartz inclusions. The maximum observed Raman shifts (either positive or negative) are also shown in Table 3. Although there is some
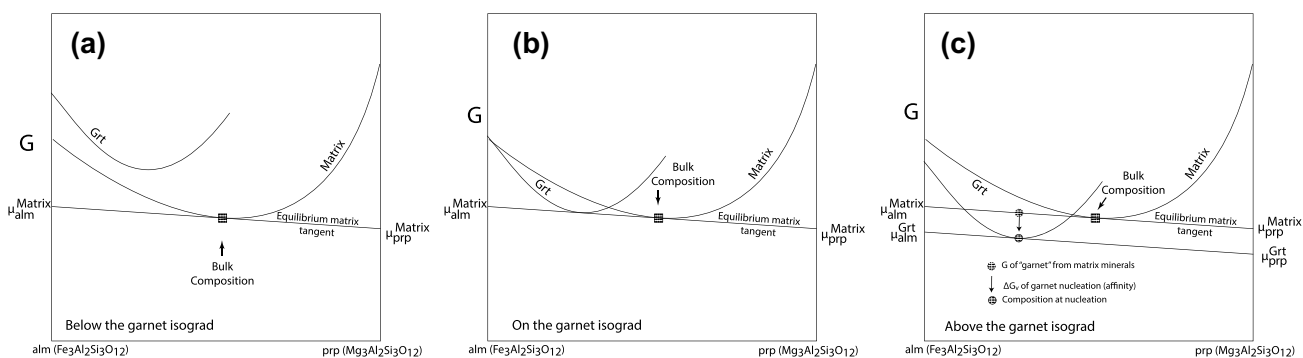

Fig. 1 Schematic G–X diagrams. **a** Diagram illustrating the G–X relationships below the garnet-in reaction. **b** Diagram illustrating the G–X relationships on the garnet-in. Note that garnet cannot nucleate because there is no driving force (affinity) for nucleation. **c** Diagram illustrating the G–X relationships above the garnet-in reaction and showing the method for calculating affinity (A) for the nucleation of garnet. The composition of the garnet that nucleates is that which gives the largest decrease in free energy. The graphical constraint on this condition is that the tangent to the matrix assemblage and garnet free-energy curves must be parallel. The mathematical solution is given in Spear et al. (2014)
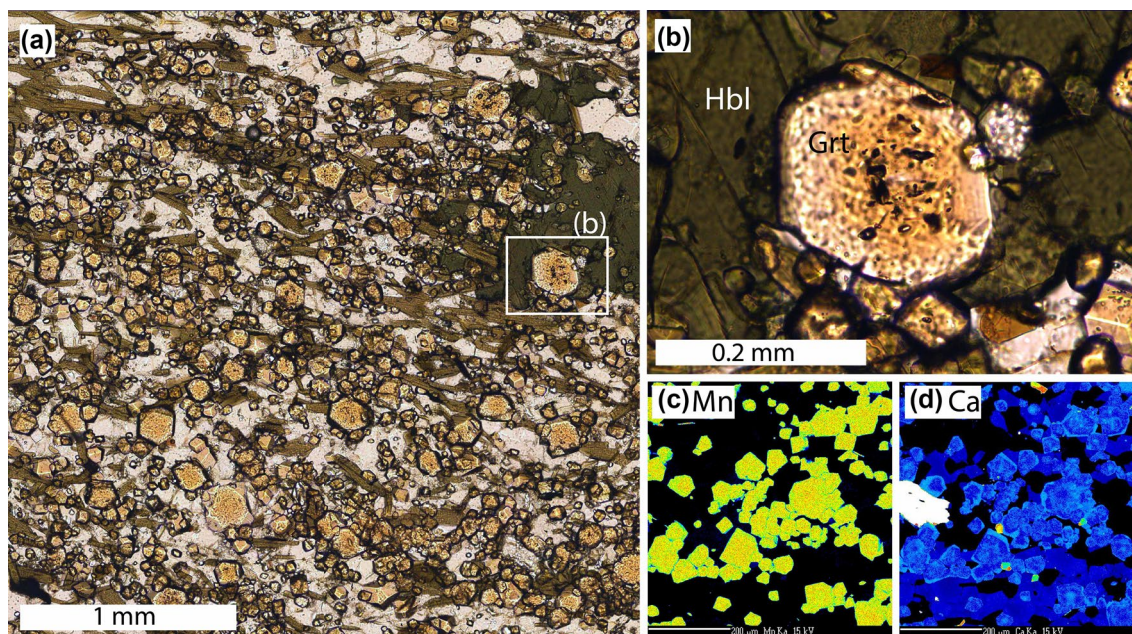
Fig. 2 Images for sample 77-51b, locality 1. **a** Photomicrograph depicting density and size range of garnet. White square shows garnet in (**b**). **b** Close up of garnet. Note inclusion-rich center and inclusion-free rim. **c** X-ray map of Mn. **d** X-ray map of Ca

scatter, it appears that in each locality the maximum Raman shifts are similar regardless of the nucleation density. For example, samples from localities 1, 2 and 3 have shifts of the 464 cm^{-1} peak of 0.5 to 0.8, 2.8 to 3.3, and -0.7 to -2.0 cm^{-1}, respectively. The uncertainty in these measurements is on the order of ± 0.3 cm^{-1} so the maximum shifts from locality 1 are statistically identical. There is a greater spread in the shifts from localities 2 and 3, but the variation only translates to a difference in the pressure of the calculated isomeke of around 0.1 GPa (see below). These measurements are consistent with the interpretation that garnet from each locality formed along similar QuiG isomekes.

Metamorphic P–T conditions were also constrained by application of garnet–biotite or garnet–hornblende thermometry and garnet–plagioclase barometry, where applicable (Figs. 8, 9, 10; Tables 4 and 5). Garnet–hornblende and garnet–biotite thermometry in samples from locality 1 (77-51b and 79-149d, respectively) using garnet rim compositions yield temperatures of around 575–600 °C at the pressure of the QuiG isomeke (gray parallelogram in Fig. 8). Garnet–plagioclase–kyanite–quartz barometry in sample 79-149d using rim compositions of garnet and plagioclase records pressure 1–1.5 kbar lower than that recorded by QuiG barometry at the same temperatures (dotted pattern in Fig. 8) and pressure calculated using garnet core composition (Table 5) and the composition of plagioclase inclusions in the garnet core (horizontal rule pattern in Fig. 8) record pressure around 1 kb higher than those determined from QuiG barometry. This difference in pressure between the

core thermo-barometry and the QuiG isomeke is within the uncertainty of the two techniques and the pressure of garnet formation is interpreted to be 0.675 ± 0.05 GPa (black star in Fig. 8). Sample 79-149d also contains staurolite and kyanite and the inferred peak P–T conditions fall below the calculated equilibrium stability for both these phases. A possible reconciliation of this apparent conundrum is that staurolite and kyanite did not form from assemblages that contain garnet, as predicted from the equilibrium calculations, but rather nucleated directly from chlorite-bearing assemblages at slightly lower temperature than predicted from the equilibrium calculations.

In locality 2 (Fig. 9), garnet–biotite temperatures using garnet rim compositions are 535 °C and 585 °C at 1.0 GPa in samples OW-17b and OW-17 m, respectively. Pressures calculated for sample OW-17 m from garnet–plagioclase–muscovite–biotite barometry for the garnet rim compositions fall below pressures inferred from QuiG barometry (dotted pattern in Fig. 9b) whereas those calculated for garnet core compositions plot around 1 kb above the QuiG isomekes (horizontal rule in Fig. 9b). Nevertheless, the QuiG isomekes for both the LoCD and HiCD samples are similar, suggesting that garnet in each sample formed at similar P–T conditions (black star in Fig. 9).

The results from locality 3 (Fig. 10) are somewhat less systematic. This is the only locality in which the measured Raman shifts of the 464 cm^{-1} peak in quartz are negative and the values in the suite of five samples range from $+0.5$ to -2.1 (Fig. 11) with the maximum negative shifts range from
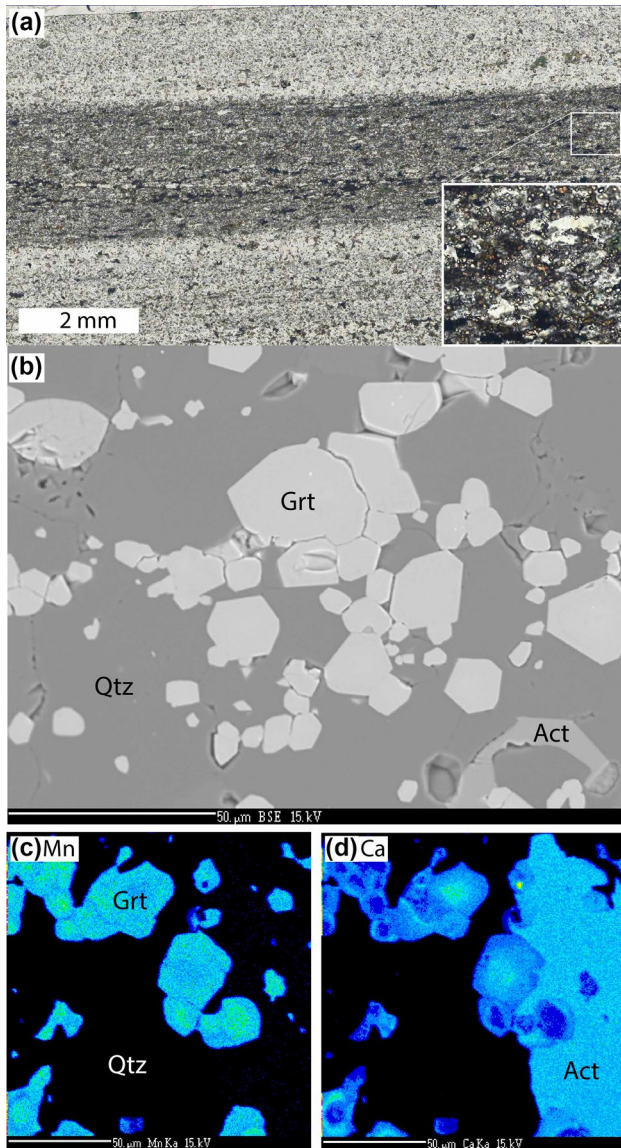
Fig. 3 Images for sample 79-103i, locality 3. **a** Photomicrograph showing well-layered, quartz-rich nature of the sample. Inset (white box) shows enlargement of a small area to better illustrate the abundance of garnet crystals. **b** BSE image showing density and size distribution of garnet crystals. **c** X-ray map of Mn. **d** X-ray map of Ca

Fig. 4 Images for sample 79-112c, locality 3. **a** BSE image showing size distribution of garnet crystals. **b** X-ray map of Mn. (c) X-ray map of Ca

Fig. 5 Images for sample 79-114c, locality 3. **a** BSE image showing size distribution of garnet crystals. **b** X-ray map of Mn. **c** X-ray map of Ca

-0.7 to -2.0 cm^{-1} (Table 3 and Fig. 11). It was assumed for the other two localities that the maximum positive shifts most faithfully recorded the conditions of garnet formation based on the assumption that any modification of the inclusion/host conditions (e.g., local fracturing or plastic flow) would relax the strains on the inclusion and move the shift toward zero. However, the Raman shift data from locality 3 suggest that garnet may have formed as P–T conditions, and hence the Raman shifts, evolved. First, it is noted that there is a good correlation between the Raman shifts of the 464 cm^{-1} and 128 cm^{-1} peaks (Fig. 11), suggesting that
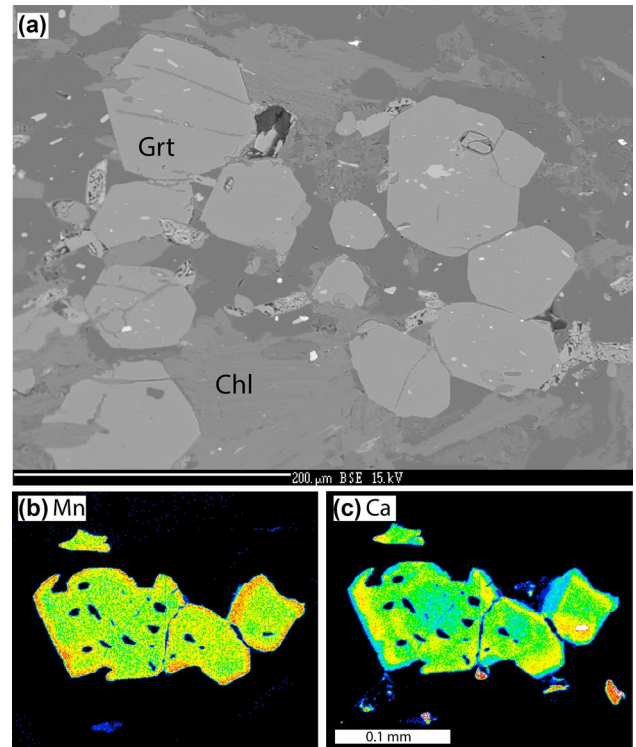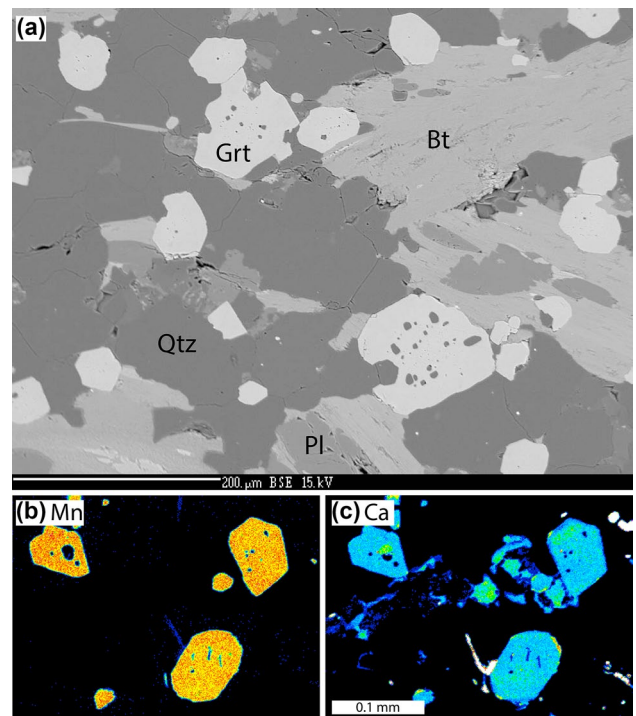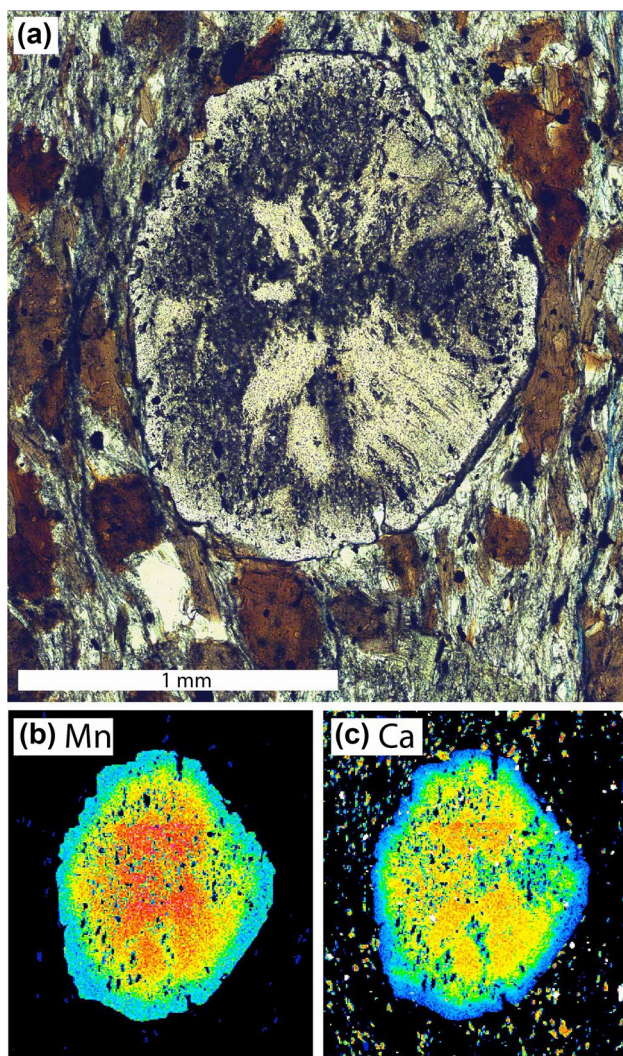
Fig. 6 Images for LoCD sample 79-115b, locality 3. **a** Photomicrograph of garnet. **b** X-ray map of Mn. **c** X-ray map of Ca. Note abundant quartz inclusions in garnet

strain relaxation, if it occurred, did so symmetrically. Second, plots of the shift of the 464 cm^{-1} Raman peak versus position in the garnet crystal suggest that for sample 79-115c the shift becomes progressively negative from core to rim (Fig. 12b). Significantly, in sample 79-115b, no such correlation is observed (Fig. 12a). The preferred interpretation of these data is that garnet formed along the isomeke where the Raman shift was close to zero and the rock then changed P–T conditions to the isomeke where the Raman shift was -2.

Garnet–plagioclase–muscovite–biotite geo-barometry also supports the interpretation that garnet from samples 79-115b and 79-115c initially formed at conditions along the isomeke where the Raman shift was approximately zero. As illustrated in Fig. 10d and e, barometry using garnet and plagioclase core compositions (dotted lines) indicate P–T

conditions similar to the zero shift isomeke (dashed line) whereas thermo-barometry using the garnet, biotite, and plagioclase rim compositions (gray parallelograms in Fig. 10d, e) indicate P–T conditions similar to the isomekes for the maximum negative shift (solid black lines). Furthermore, sample 79-115c contains staurolite and the calculated stability field for staurolite (Fig. 10e, light gray-shaded area) is located at higher temperature and pressure than the garnet rim geo-thermo-barometry and the isomekes for the maximum negative Raman shifts. Therefore, it is interpreted that garnet from the LoCD samples 79-115b and 79-115c formed at approximately 625 °C, 0.65 GPa (black stars) and the samples then evolved toward lower pressure and higher temperature (black arrow and open stars in Fig. 10).

The Raman shifts for the HiCD samples (Figs. 10a, b, c and 11) range from near zero to maximum values of − 0.6 to − 1.0 and the corresponding maximum isomekes (black lines in Fig. 10) fall at higher pressures than those for the LoCD samples. It is unclear whether the spread of Raman shifts reflect garnet formation under different P–T conditions, or a resetting of Raman shifts that were initially zero. However, it is clear that the LoCD samples formed garnet at conditions near the black star (Fig. 10d, e) and it will be assumed that garnet in all samples formed at similar P–T conditions and was then reset to various degrees as the rocks evolved toward the lower-pressure conditions (open stars in Fig. 10). It should be pointed out that this assumption does not impact the main conclusion of this study that garnet formation in the HiCD and LoCD samples occurred at significantly different degrees of overstepping.

Figures 8, 9, 10 also show contours of calculated affinity. As discussed in the Methods section, affinity is calculated as the difference in free energy between the tangent plane defined by the matrix assemblage at the P–T conditions of interest and the free energy of a fictive garnet crystal constrained to lie on a plane parallel to the tangent plane defined by the matrix assemblage (i.e., Fig. 1). In each diagram, the line with a calculated affinity of zero is the garnet-in line and positive value of affinity (kJ/mol-O) are quantifications of the degree of overstepping of the garnet-in reaction. Owing to the high MnO content of many of the HiCD samples, the calculated position of the equilibrium garnet-in line (corresponding to an affinity of zero) is at a very low T and P, in many instances, does not plot on the diagram. The affinity in Figs. 8, 9, 10 was calculated using the SPaC thermodynamic dataset (Spear and Pyle 2010), but similar diagrams were also calculated using the HP11 (ds6.2) and HP98 (ds5.5) datasets (see supplemental material). In every case, the calculated garnet-in line falls at lower T and P using the HP11 or HP98 datasets and the affinities calculated at the inferred conditions of garnet formation (black stars in Figs. 8, 9, 10) are significantly larger. For example, in sample 77-51b, the affinity at garnet nucleation using the HP11 ds6.2 dataset
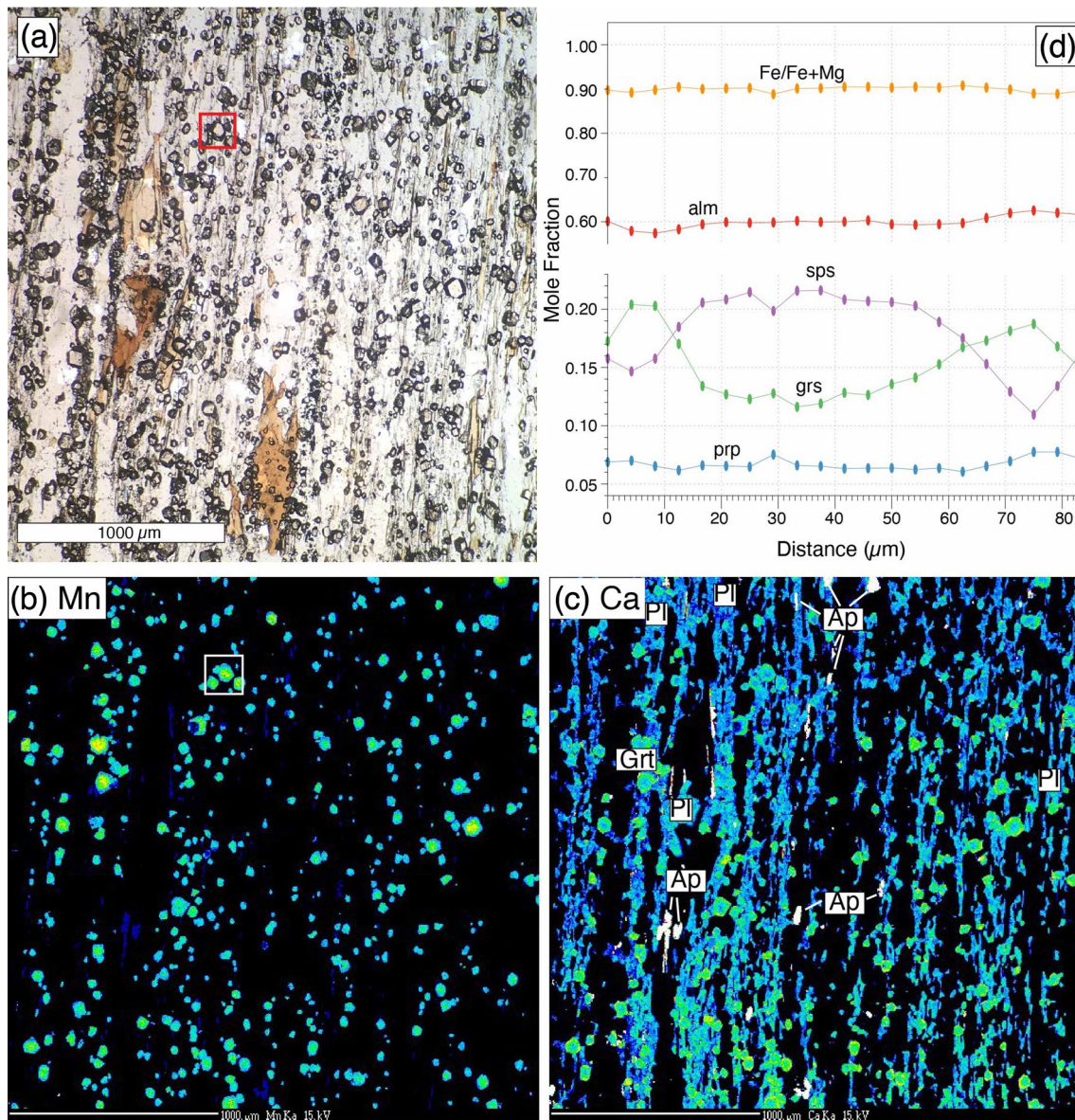
Fig. 7 Sample OW-17b, locality 2. **a** Photomicrograph showing density and size distribution of garnet. **b** X-ray map of Mn. **c** X-ray map of Ca. **d** Line traverse of garnet outlined in (**a**) and (**b**). Note systematic decrease in Mn and increase then decrease in Ca distribution

is around 4.5 kJ/mol-O as opposed to around 2.8 kJ/mol-O using the SPaC dataset (Table 3). Therefore, using the SPaC dataset results in a minimum estimate of the affinity at garnet nucleation. It can be noted that the difference in calculated results between the SPaC, HP11, and HP98 datasets lies principally in the thermodynamic properties (enthalpy and activity model) of spessartine garnet. Additional experimental data on Mn-rich garnet would be needed to better constrain the calculated stability of garnet and affinities.

The calculated affinities at the inferred P–T conditions of garnet formation (black stars in Figs. 8, 9, 10) are listed in Table 3 for both the SPaC and HP11 datasets. Affinities calculated from the SPaC dataset range from around 150

to 500 J/mol-O for the LoCD samples up to nearly 4300 J/mol-O for the HiCD samples. If the interpretation is correct that garnet in both the LoCD and HiCD samples formed at similar P–T conditions, this implies significant difference in the degree of overstepping at the point of garnet nucleation. Similarly, if the P–T conditions are similar, then this would also suggest that the time of garnet nucleation was the same, or at least similar, in each locality. An additional line of evidence also suggests that the HiCD and LoCD samples nucleated garnet at similar P–T conditions and similar times. Each sample displays a well-defined fabric and, in all cases, garnet appears to have nucleated either during or after the development of this fabric. For example, the LoCD sample

Table 3 Raman shifts of quartz inclusions in garnet, calculated P&T and affinity

Sample	Type	Number of inclusions measured	Max Raman shift 464	Max Raman shift 206	Max Raman shift 128	T at nucleation (°C)	P at nucleation (GPa)	Affinity at nucleation (kJ/mol-O) SPaC	Affinity at nucleation (kJ/mol-O) HP11
Locality 1									
77-51b	HiCD	17	0.8	1.8	0.1	580	0.670	2.8	4.5
79-149d	LoCD	13	0.5	3.65	0.35	580	0.670	0.15	0.65
Locality 2									
OW-17b	HiCD	14	3.3	10.3	2.5	600	1	1.5	3.0
OW-17 m	LoCD	18	2.8	10.1	2.6	600	1	0.5	1.2
Locality 3									
79-103i	HiCD	12	− 0.7	− 1.68	− 0.7	575	0.45	4.3	6.1
79-112c	HiCD	16	− 0.85	− 1.67	− 1.45	575	0.45	2.15	3.6
79-114c	HiCD	9	− 1	− 1.24	− 1.1	575	0.45	1.4	4.3
79-115b	LoCD	21	− 2	− 5.7	− 2	575	0.45	0.5	1.8
79-115c	LoCD	6	− 1.75	− 5.7	− 2	575	0.45	0.15	0.85

79-149d from locality 1 has inclusion trails of quartz that define a weak spiral suggesting syn-deformational growth. Garnet from the HiCD sample from the same locality (79-51b) appears to have overgrown the fabric defined by the orientation of hornblende and biotite, suggesting post-deformational growth. Similarly, garnet from the LoCD sample
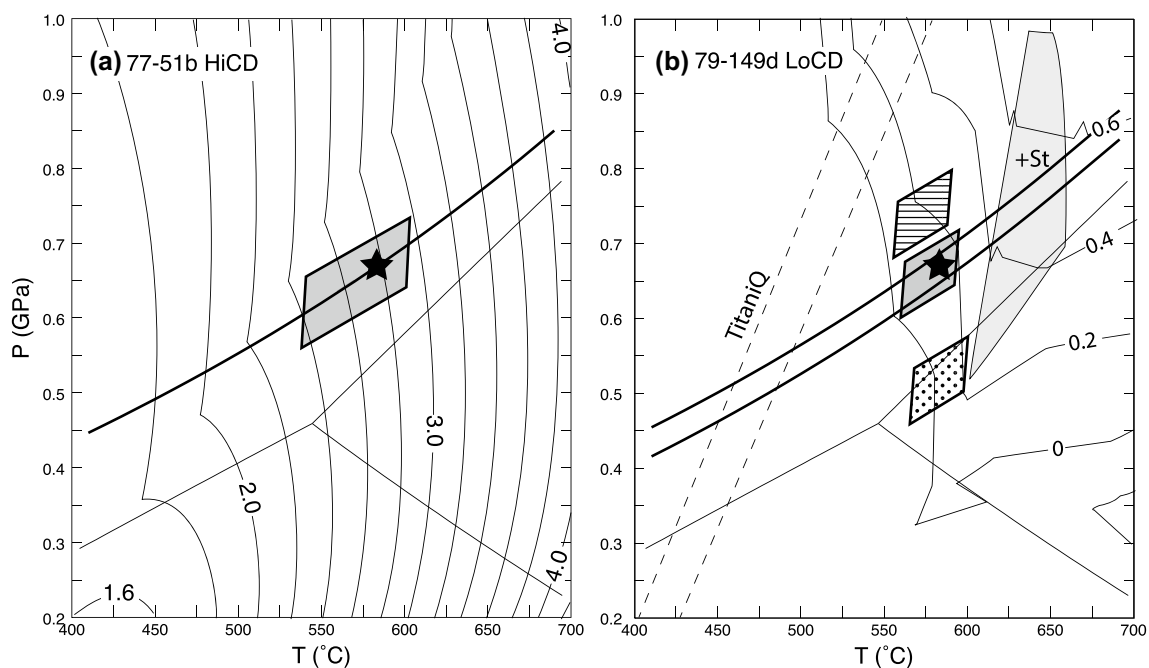

Fig. 8 P–T diagrams contoured for affinity for samples from locality 1. **a** 77-51b; **b** 79-149d. Values of affinity are in kJ/mol-O. Heavy lines are the isomekes for quartz-in-garnet (QuiG) barometry. Dashed lines in **b** are from Ti in quartz thermometry (TitaniQ). Gray parallelograms are temperatures inferred from garnet–biotite or garnet–hornblende thermometry with pressure constrained by QuiG barometry. Dotted and horizontally ruled parallelograms display P–T conditions calculated using garnet rim and garnet core compositions, respectively. Black star indicates the inferred conditions of garnet nucleation. The calculated stability field for staurolite in sample 79-149d is shown with light gray shading. All calculations of phase boundaries and affinities were done using the SPaC dataset and the bulk compositions listed in Table 4. Results of similar calculations using the HP98 and HP11 datasets are presented in the supplemental material (Online Resources 2 and 3)
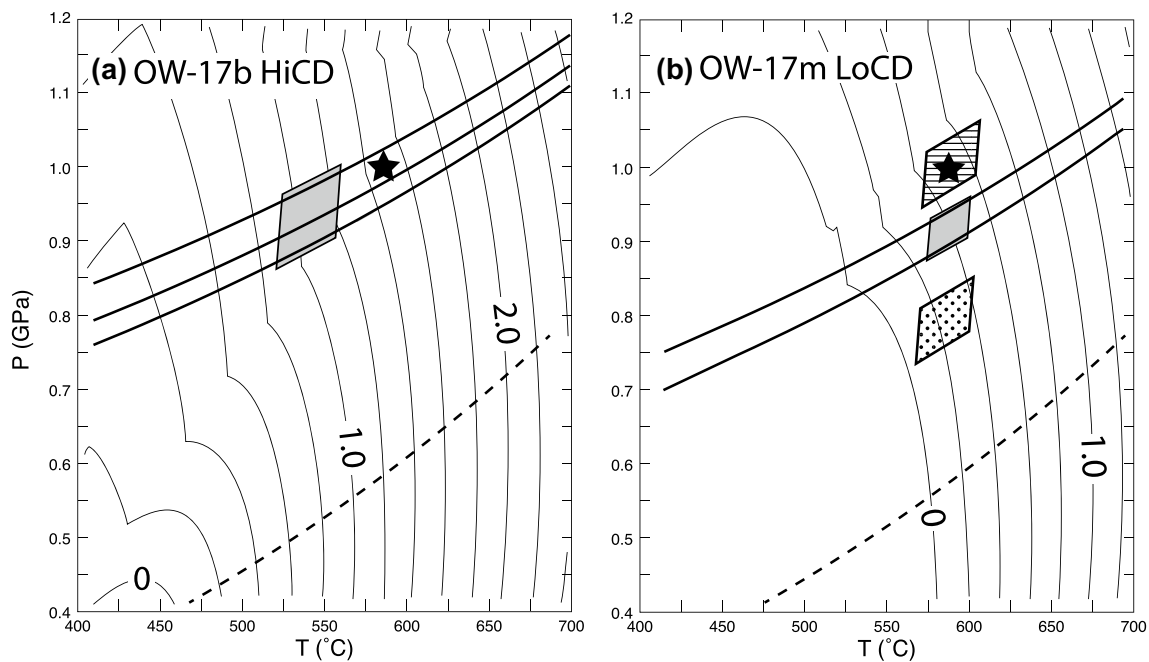
Fig. 9 P–T diagrams contoured for affinity for samples from locality 2. **a** OW-17b; **b** OW-17 m. Values of affinity are in kJ/mol-O. Heavy lines are the isomekes for quartz-in-garnet (QuiG) barometry. Gray parallelograms outline temperatures inferred from garnet–biotite ther-mometry with pressure constrained by QuiG barometry. Black star indicates the inferred conditions of garnet nucleation. Dashed line is the isomeke for 0 Raman shift

79-115b (locality 2: Fig. 6) appears to have overgrown a quartz fabric and garnet from the HiCD samples from the same locality (79-103i, 79-112c and 79-114c, Figs. 3, 4, 5) are undisturbed by fabric development again suggesting post-deformational growth. Indeed, sample 79-103i contains an isoclinal fold (not shown) and garnet is undisturbed by this fold.

Discussion

Theoretical background

The approach taken here will follow on the theory of homogeneous nucleation (e.g., McLean 1965; Ridley and Thompson 1986; Kelly et al. 2013) even though it is most likely that garnet nucleation is more appropriately described as heterogeneous nucleation. Implications for garnet nucleation based on considerations of heterogeneous nucleation theory will be examined below.

Nucleation of a porphyroblast requires overcoming the activation energy barrier. Classical nucleation theory predicts the nucleation rate (R) to be an exponential function of this activation energy (ΔG^*):

$$R = C\exp\left(\frac{-\Delta G^*}{kT}\right) \tag{1}$$

where C is a constant that is a function of the number of nucleation sites, a probability factor, and a rate constant, k is the Boltzmann constant, and T is temperature. The activation energy is composed of a competition between three terms: a volumetric energy (ΔG_v: always negative) that is the difference between the free energy of a metastable matrix assemblage and the free energy of the nucleated phase at the same conditions, a strain energy (ΔG_s), and a surface energy (σ: always positive) of the nucleus:

$$\Delta G^* = \frac{4}{3}\pi r^3\left(\Delta G_v + \Delta G_s\right) + 4\pi r^2\sigma \tag{2}$$

Note that the strain energy ΔG_s can be either positive or negative. A positive strain energy is caused by crystallographic mismatch between the nucleus and adjacent crystals and works against nucleation and a negative strain energy results from deformation of the matrix crystals and works in favor of nucleation of a new phase.

The critical radius (r^*) occurs at the maximum of the plot of ΔG^* versus r (Fig. 13):

$$r^* = -\frac{2\sigma}{\left(\Delta G_v + \Delta G_s\right)} \tag{3}$$

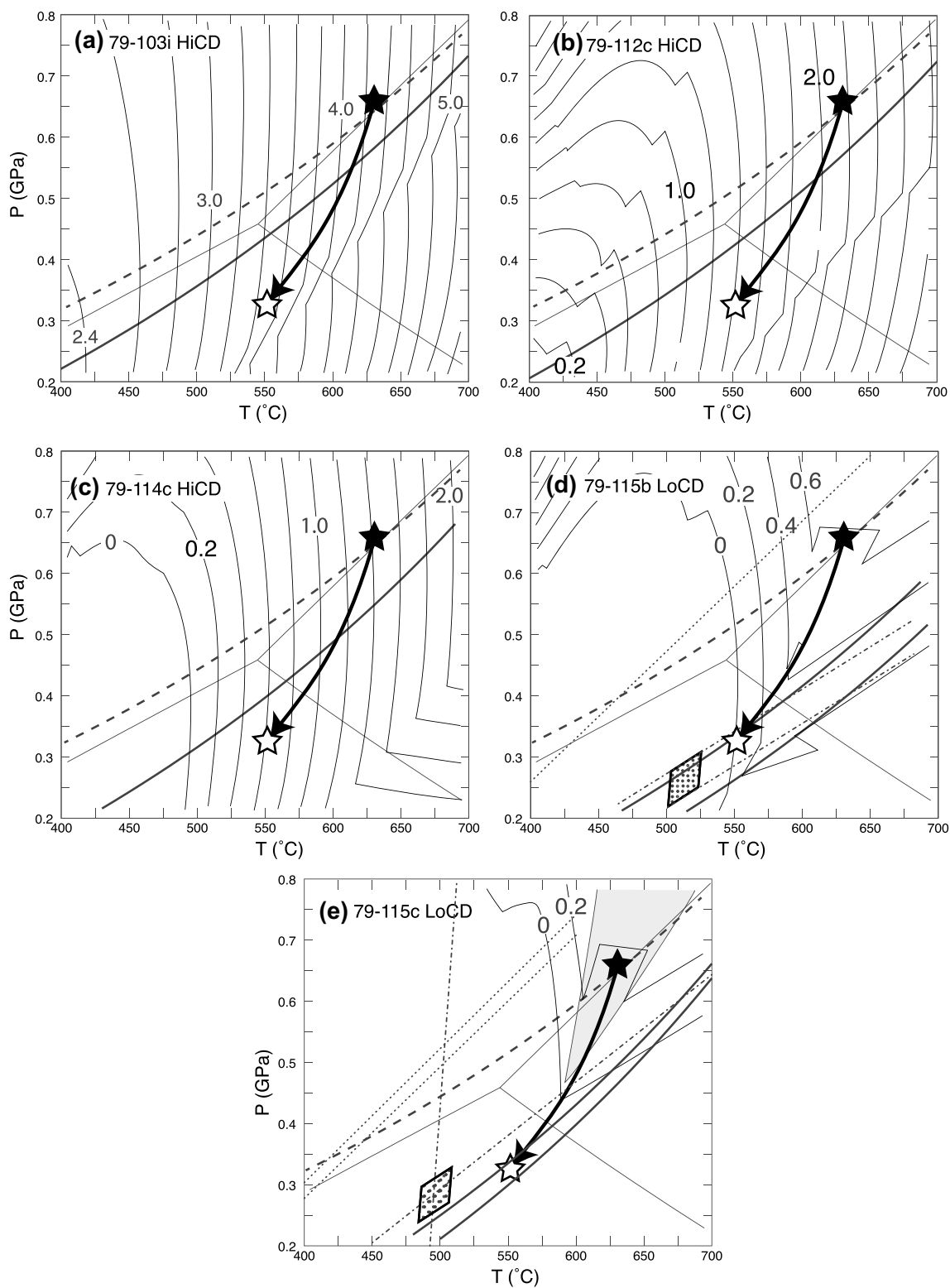Substituting Eq. (3) into Eq. (2) yields the free energy at the top of the nucleation barrier:

Fig. 10 P–T diagrams contoured for affinity for samples from locality 3. **a** 79-103i; **b** 79-112c; **c** 79-114c; **d** 79-115b; **e** 79-115c. Values of affinity are in kJ/mol-O. Heavy lines are the isomekes for quartz-in-garnet (QuiG) barometry showing the maximum negative shift. Dashed lines are the isomekes for 0 Raman shift. Parallelogram with dotted fill in (**d**) and (**e**) shows the intersection of garnet–biotite thermometry and garnet–plagioclase barometry using rim compositions. Black star indicates the inferred conditions of garnet nucleation and open star shows P–T conditions along the uplift path (black arrow). The calculated stability field for staurolite in sample 79-115c is shown with light gray shading
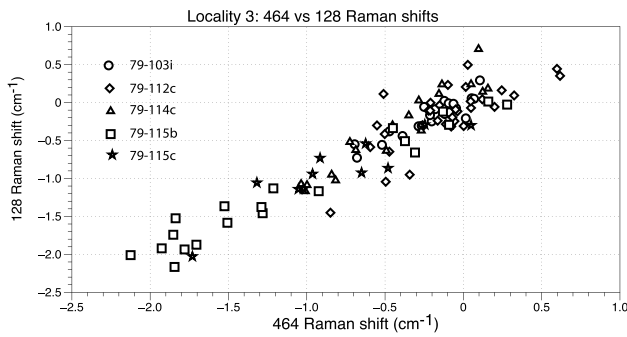
Fig. 11 Plot of the Raman shift of the 464 cm^{-1} peak versus the Raman shift of the 128 cm^{-1} peak for all samples from locality 3
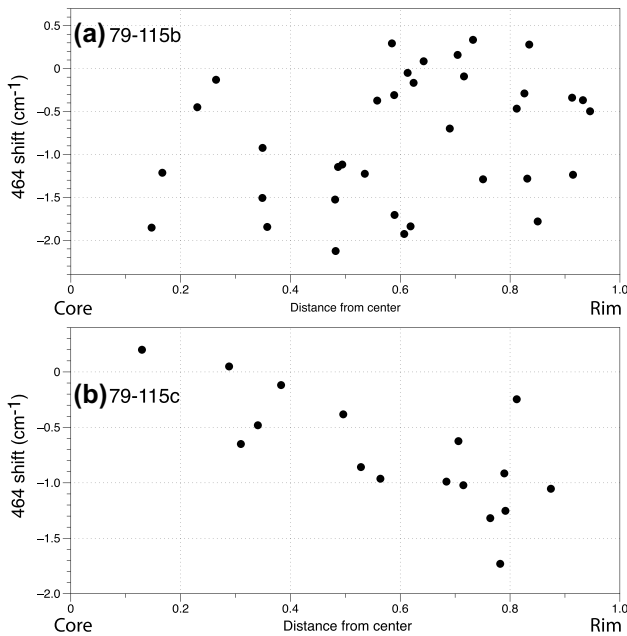

Fig. 12 Plots of normalized distance from the garnet center versus the shift of the 464 cm^{-1} Raman peak. **a** Sample 79-115b; **b** Sample 79-115c. Note the lack of correlation with position for sample 79-115b

$$\Delta G_n^* = \frac{16\pi\sigma^3}{3\left(\Delta G_v + \Delta G_s\right)^2} \quad (4)$$

Quantification of the strain (ΔG_s) and surface energies (σ) is difficult but neither is likely to be a strong function of the degree of overstepping. On the other hand, ΔG_v is a first order function of overstepping due to the relationship between G, T and P:

$$dG_v = -\Delta S dT + \Delta V dP \quad (5)$$

Ignoring the strain energy, the critical energy barrier (ΔG_n^*) will, to a first order, be an inverse function of the square of ΔG_v and will vary with P and T as indicated in

Eq. (5). The nucleation rate, being an exponential function of the ΔG^* will thus vary dramatically with the magnitude of ΔG_v. Assuming for the moment that ΔS and ΔV are constant, Eq. (5) can be integrated between the equilibrium P and T of garnet formation (the garnet-in reaction) and the actual P and T of garnet nucleation to give:

$$\Delta G_v = -\Delta S \Delta T + \Delta V \Delta P$$

where ΔT and ΔP are the pressure and temperature of overstepping. Substituting into Eq. (4) (again neglecting the strain energy) yields

$$\Delta G_n^* = \frac{16\pi\sigma^3}{3(-\Delta S \Delta T + \Delta V \Delta P)^2} \quad (6)$$

In other words, the activation energy term for nucleation, ΔG_n^*, in (1) is proportional to the exponential of the inverse of the square of the temperature and pressure of overstepping. As been pointed out by numerous authors, this relationship results in a dramatic increase in the nucleation rate over just a few degrees to several tens of degrees of overstepping (e.g., Ridley and Thompson [1986]; Kelly et al. [2013]; Pattison et al. [2011]).

In this communication, the value of ΔG_v is taken to be the negative of the affinity calculated using the MDF approach (see "Methods" section), which includes overstepping in both temperature and pressure. Inasmuch as the affinity is calculated in J/mol-O, conversion to a volumetric free energy change is done using the molar volume of garnet.

Application

If the P–T conditions at which garnet nucleated in the HiCD and LoCD samples are approximately correct, then the affinity for garnet nucleation in the HiCD samples was around an order of magnitude greater than that in the LoCD samples. This conclusion is valid regardless of the thermodynamic dataset used (SPaC, HP98 or HP11), although the magnitudes of affinity are greater with calculations using HP98 or HP11. The question to be addressed now is whether this difference in affinity can account for the dramatically different crystal densities. To compare theoretical analysis above with the observed, it is necessary to make an assumption about the time interval (Δt) over which the nucleation occurred. That is, combining Eqs. (1) and (4) we have (ignoring strain energy):

$$R = C\exp\left(\frac{-16\pi\sigma^3/3\Delta G_v^2}{kT}\right) \quad (7)$$

from which

Table 4 Bulk chemical analyses of samples studied

	Locality 1		Locality 2		Locality 3				
	HiCD 77-51b	LoCD 79-149d	HiCD OW-17b	LoCD OW-17 m	HiCD 79-103i	HiCD 79-112c	HiCD 79-114c	LoCD 79-115b	LoCD 79-115c
SiO_2	66.59	59.26	78.01	37.93	84.12	90.70	73.72	62.25	63.91
Al_2O_3	11.74	18.28	10.93	20.54	4.03	4.16	9.28	18.48	17.55
TiO_2	0.47	1.05	0.49	3.43	0.06	0.11	0.54	0.86	0.93
MgO	1.99	5.10	1.25	9.01	0.85	0.76	2.01	3.12	3.44
FeO	8.80	9.59	4.24	23.11	4.84	2.17	8.66	7.53	7.86
MnO	3.60	0.20	0.49	0.45	3.58	0.43	0.59	0.42	0.22
CaO	3.15	0.30	0.91	1.70	2.48	0.81	0.82	1.19	0.95
Na_2O	2.36	0.78	1.16	2.00	0.04	0.49	1.63	1.38	1.04
K_2O	1.30	5.44	2.52	1.82	0.00	0.37	2.75	4.77	4.1
	100.00	100.00	100.00	100.00	100.00	100.00	100.00	100.00	100.00
SiO_2-free normalization									
Al_2O_3	35.14	44.87	49.70	33.10	25.38	44.73	35.31	48.95	48.63
TiO_2	1.41	2.58	2.23	5.53	0.38	1.18	2.05	2.28	2.58
MgO	5.96	12.52	5.68	14.52	5.35	8.17	7.65	8.26	9.53
FeO	26.34	23.54	19.28	37.24	30.48	23.33	32.95	19.95	21.78
MnO	10.78	0.49	2.23	0.73	22.54	4.62	2.25	1.11	0.61
CaO	9.43	0.74	4.14	2.74	15.62	8.71	3.12	3.15	2.63
Na_2O	7.06	1.91	5.28	3.22	0.25	5.27	6.20	3.66	2.88
K_2O	3.89	13.35	11.46	2.93	0.00	3.98	10.46	12.64	11.36

Table 5 Representative analyses of selected garnet cores

	77-51b	79-149d	OW-17b	OW-17 m	79-103i	79-115b	79-115b
SiO_2	38.29	36.98	36.54	36.45	37.28	36.99	36.33
TiO_2	–	–	0.12	0.08	0.11	0.21	0.07
Al_2O_3	19.37	21.40	21.40	21.17	20.62	21.39	21.51
FeO	20.80	30.18	26.39	29.33	14.73	22.34	23.47
MnO	14.92	5.55	10.46	5.03	18.45	13.72	13.15
MgO	1.60	3.10	1.46	1.54	0.45	1.10	1.43
CaO	5.59	2.60	4.04	6.37	10.42	6.00	4.87
Total	100.78	99.80	100.50	100.01	102.08	101.77	100.88
Prp	0.062	0.123	0.058	0.061	0.017	0.043	0.056
Alm	0.453	0.676	0.590	0.647	0.310	0.487	0.515
Sps	0.329	0.126	0.237	0.112	0.393	0.303	0.292
Grs	0.156	0.075	0.116	0.180	0.281	0.168	0.137
Fe/(Fe + Mg)	0.880	0.845	0.910	0.914	0.948	0.919	0.902

$$\text{Number of crystals} = \Delta tR = \Delta tC\exp\left(\frac{-16\pi\sigma^3/3\Delta G_v^2}{kT}\right) \tag{8}$$

Assuming all nuclei formed over the same time interval and the constant C is the same for all samples, it is possible to explore how well crystal density aligns with the predictions of nucleation theory by evaluating the value of ΔtC that would provide the observed range of crystal densities. Figure 14 show plots of the number of garnet crystals/cm³ plotted against the affinity at the P–T conditions of nucleation as determined from Figs. 8, 9, 10 (Table 3) for calculations done with both the SPaC and HP11 datasets (results from the HP98 dataset would plot between these two). In this plot, the affinity has been converted from units of J/mol-O to J/cm³ using the molar volume of almandine of 115 cm³/mole (12 oxygens: conversion factor = 9.583). As discussed above, samples with fewer garnet crystals record significantly lower values of affinity at garnet nucleation. Note that the Y-axis is a logarithmic scale so uncertainties in the garnet crystal densities do not significantly impact the results. Also shown is a plot of Eq. 8 (solid line). The
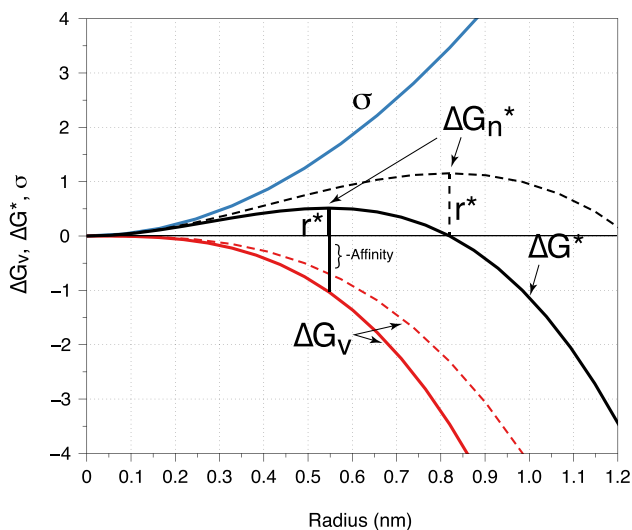
Fig. 13 Plot of nucleus radius versus ΔG_v (volumetric energy for the production of a new nucleus), σ (surface energy), and ΔG^* (sum of volumetric and surface energies; Eq. 2). Dashed lines represent a small degree of overstepping; solid lines represent a larger degree of overstepping. Note that the critical radius (r^*) is smaller with a larger degree of overstepping. Energy units are arbitrary
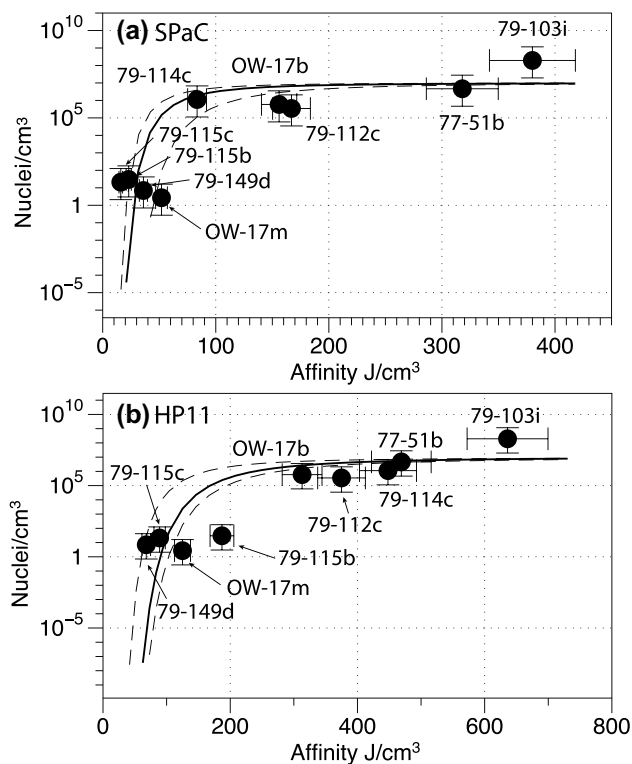

Fig. 14 Plot of affinity (J/cm^3) versus number of nuclei/cm^3 based on data in Tables 2 and 3 and Figs. 8, 9, 10. **a** Affinities based on calculations using the SPaC dataset; **b** Affinities based on calculations using the HP11 dataset. Solid curves are calculated from Eq. 8 using the preferred values of surface energy. Dash curves are calculated from Eq. 8 using minimum and maximum values of surface energies (0.18, 0.03 and 0.035, 0.05, respectively)

value of ΔtC has been adjusted to 10^7 to match the samples with the largest number of crystals (note the curve levels off at 10^7 crystals/cm^3). Samples with low numbers of crystals record affinities around 25 J/cm^3 (SPaC) or 100 J/cm^3 (HP11). The location of the steep part of the curve is highly sensitive to the value of surface energy (σ) because of the cubed dependence on this quantity. Values of the surface energy were varied and it was found that the values that best fits the SPaC data is 0.018–0.03 J/m^2 with a preferred value of 0.022 J/m^2 and the value that best fits the HP11 data is 0.035–0.05 with a preferred value of 0.045. For comparison, previous studies have estimated interfacial energies to be 0.01–0.1 J/m^2 (Ridley and Thompson 1986), 0.03–0.3 J/m^2 (Gaidies et al. 2011), and 0.007–0.255 J/m^2 (Kelly et al. 2013), entirely consistent with the findings of this study.

The value of ΔtC of 10^7 is difficult to evaluate because the time over which the nucleation occurs is entirely unknown. Studies in which the ages of garnet cores and rims have been determined reveal that garnets grow relatively quickly. For example, the mean core–rim age difference of garnet from a sample from Sifnos, Greece was determined to be 40 ka with a range from effectively zero to 1 Ma (Dragovic et al. 2012). A similar study of garnet from Townshend Dam, Vermont, revealed an average garnet growth duration of 3.8 Ma, although the range could be considerably smaller (Gatewood et al. 2015). In contrast, experimental studies report significant garnet nucleation in a matter of hours (e.g., Thomas and Spear 2018). Taking the extremes of 1 h and 1 Ma for Δt, the value of C would range from 3×10^3 to 3×10^{-7}/sec.

Alternatively, one can evaluate the time it takes to grow a garnet of a certain size based on published estimates of garnet growth rates. The growth rates determined by Christensen et al. (1989), Schmidt et al. (2015), and Dragovic et al. (2012) range from around 0.25 to 250 mm/Ma. Based on this range, the time required to make a garnet of 10 μm diameter (the average size of garnet in sample 79-103i) is 20–20 k years, which suggests that nucleation in the coticule samples occurred over very short time spans. Using this range for Δt and a value of $\Delta tC = 10^7$, the value of C ranges from 1.6×10^{-2}/sec to 1.6×10^{-5}/sec.

According to classical nucleation theory, the constant C is the product of the number of potential nucleation sites (N_s) times the probability that a critical nucleus of radius r^* will continue to grow (Z) times an atomic jump frequency factor (υ):

$$C = N_s Z \nu$$

In metamorphic rocks, there is a finite number of nucleation sites. For example, it is not possible to nucleate a garnet in the interior of another phase such as quartz. It is proposed that the most probable nucleation sites are grain boundaries at which several phases are in contact. For the

nucleation of garnet from an assemblage of quartz + muscovite + biotite + chlorite + plagioclase + ilmenite, a likely set of phases would include chlorite (to supply Al, Fe and Mg), plagioclase (to supply Ca) and ilmenite (to supply Mn). If assumptions are made about grain size and the configuration of crystals, it is possible to calculate the number of potential nucleation sites in a rock of any specified modal mineralogy. Using sample 79-103i as an example (Table 6), the modal mineralogy (garnet-free) at the conditions of garnet nucleation was calculated using the measured bulk composition. If an average grain size of 10 μm (diameter) is assumed, then the probability of one of the five possible 4-phase nodes ranges from around 3×10^{-7} to 3×10^{-4} with the most probable assemblage being quartz + chlorite + zoisite + actinolite. Assemblages that include ilmenite have a cumulative probability of only around 7×10^{-6} because of the small modal amount of ilmenite. A rock consisting of crystals with a diameter of 10 μm contains around 1.9×10^{9} crystals. Assuming hexagonal close packing (which admittedly leaves void space), each crystal contributes to 6, 4-crystal nodes so the total number of 4-crystal nodes in 1 cm^3 is around 2.8×10^{9}. Given a cumulative probability of 3×10^{-4} for a 4-phase node in which all phases are different, this yields a total of only 9×10^{5}/cm^3 potential nucleation sites. The actual number of garnet nuclei in sample 79-103i is closer to 2×10^{8}, which suggests that many other 4-phase nodes (e.g., ones that contain 2 or more of the same phase) were accessible as nucleation sites. Indeed, microscopic examination of sample 79-103i reveal garnet crystals aligned along what appear to be healed fractures within quartz grains, so it is evidently possible to nucleate garnet along grain boundaries and fractures within a single phase such as quartz if the affinity is sufficiently high. At the other extreme, sample 79-149d contains only around 7 nuclei/cm^3. Using the calculated modal mineralogy in the garnet-free assemblage and assuming an average grain size of 1 mm, the number of 4-phase nodes in which all phases are distinct is 18, which is of the same order as the actual number of garnet crystals.

Equation 3 describes the critical radius at the top of the nucleation energy barrier. Using the value of surface energy

(sigma) inferred from Fig. 14 of 0.018 J/m^2 and the value of ΔGv calculated from the estimates of affinity at the conditions of garnet nucleation, values of the critical radius have been calculated. Values of $r*$ range from 0.091 nm (sample 79-103i) to 1.7 nm (samples 79-149d and 79-115b). Using the molar volume of almandine of 115 cm^3/mole, the number of atoms (cations plus oxygen) in a critical nucleus ranges from 0.8 (sample 79-103i) to around 2300 (samples 79-149d and 79-115b). Clearly, a critical radius of the order 0.1 nm is too small because it is on the order of the radius of an oxygen atom and it takes more than a single oxygen atom to form a nucleus.

What are the implications of the unrealistically small critical radius? Of course, a distinct possibility is that classical nucleation theory, which applies to nuclei forming in pure materials, does not apply to nucleation in a multi-phase metamorphic rock. It is clear, however, that nucleation must have been suppressed even as affinity increases to rather large values. One possibility is that the lack of sufficient space along grain boundaries or in multi-grain nodes prevents clusters of atoms to form from random motions so additional factors leading to nucleation must be considered. The observation that rocks (HiCDs) with > 10^6 crystals/cm^3 have apparently nucleated at the same P–T conditions as rocks with only a few crystals/cm^3 (LoCDs) suggests that some external trigger might be responsible for initiating nucleation. Possible trigger mechanisms include (a) deformation and the addition of strain energy; (b) fluid influx; (c) additional energy such as might occur from an earthquake or bolide impact. It seems unlikely that strain triggered nucleation because of the textural arguments made above that the HiCD samples seem to be undisturbed by fabrics and thus probably nucleated after deformation ceased. Fluid influx seems unlikely as well because all rocks would have to have been infiltrated at the same conditions and there is no other evidence such as metasomatic effects that suggest fluids have infiltrated. An earthquake or bolide impact seems far-fetched but cannot be ruled out. Further studies that constrain the time of nuclei formation in LoCD and HiCD samples, for example using Sm–Nd dating of garnet cores, would help constrain the mechanism fostering garnet nucleation.

One argument against a nucleation trigger event is the well-documented occurrence of rocks in which garnet appears to have undergone progressive nucleation (e.g., Chernoff and Carlson 1997; George and Gaidies 2017). The fundamental observation in these studies is that garnets display a range of sizes and large garnets have higher Mn contents in their cores. Inasmuch as the Mn content of garnet is known to reflect Rayleigh depletion in the matrix as Mn is sequestered into garnet, it is assumed that the Mn content can be used as a qualitative time line, from which it follows that all garnets did not nucleate simultaneously. However, it does not necessarily follow that progressive nucleation

Table 6 Modal mineralogy and probabilities of 4-grain nodes for sample 79-103i

	Quartz	Chlorite	Ilmenite	Zoisite	Actinolite
Modes	76.78	10.94	0.07	4.69	7.52
Probability					
4-phase node	Quartz	Chlorite	Ilmenite	Zoisite	2.69E-06
	Quartz	Chlorite	Ilmenite	Actinolite	4.31E-06
	Quartz	Chlorite	Zoisite	Actinolite	2.96E-04
	Quartz	Ilmenite	Zoisite	Actinolite	1.85E-06
	Chlorite	Ilmenite	Zoisite	Actinolite	2.63E-07

requires changes in pressure and temperature as a driving force, as has been demonstrated by Spear (2017) and Spear and Wolfe (2019, 2020). Furthermore, there are few constraints on the time over which the sequential nucleation took place and it is possible that the observed examples of progressive nucleation occurred over short time scales; in other words, essentially instantaneously.

As noted above, the quantitative values derived here for the affinity at the point of nucleation are dependent on the values used in then thermodynamic calculations. Specifically, the difference in calculated affinity using the SPaC18 versus HP11 thermodynamic databases is on the order of a factor of 2, largely due to the differences in the thermodynamic properties of spessartine garnet. However, regardless of the true values, the differences in affinity between the HiCD and LoCD rocks will persist simply due to the differences in the bulk Mn contents of the rocks. Well-characterized experimental studies in systems containing manganese would be very helpful in further quantifying the amount of affinity necessary to nucleate garnet.

References

Angel RJ, Mazzucchelli ML, Alvaro M, Nestola F (2017) EosFit-Pinc: a simple GUI for host-inclusion elastic barometry. Am Miner 102:1957–1960

Castro AE, Spear FS (2016) Reaction overstepping and reevaluation of the peak P-T conditions of the blueschist unit Sifnos, Greece: implications for the Cyclades subduction zone. Int Geol Rev 59:548–562

Chernoff CB, Carlson WD (1997) Trace-element zoning in garnet: evidence for disequilibrium during garnet growth. Geol Soc Am Abstr Progr 29:338–339

Christensen JN, Rosenfeld JL, De Paolo DJ (1989) Rates of tectono-metamorphic processes from rubidium and strontium isotopes in garnet. Science 244:1465–1469

Dragovic B, Samanta LM, Baxter EF, Selverstone J (2012) Using garnet to constrain the duration and rate of water-releasing metamorphic reactions during subduction: an example from Sifnos, Greece. Chem Geol 314–317:9–22. https://doi.org/10.1016/j.chemgeo.2012.04.016

Gaidies F, Pattison DRM, de Capitani C (2011) Toward a quantitative model of metamorphic nucleation and growth. Contrib Miner Petrol 162(5):975–993. https://doi.org/10.1007/s00410-011-0635-2

Gatewood MP, Dragovic B, Stowell HH, Baxter EF, Hirsch DM, Bloom R (2015) Evaluating chemical equilibrium in metamorphic rocks using major element and Sm-Nd isotopic age zoning in garnet, Townshend Dam, Vermont, USA. Chem Geol 401:151–168

George FR, Gaidies F (2017) Characterisation of a garnet population from the Sikkim Himalaya: insights into the rates and mechanisms of porphyroblast crystallisation. Contrib Mineral Petrol. https://doi.org/10.1007/s00410-017-1372-y

Graham CM, Powell R (1984) A garnet-hornblende geothermometer: calibration, testing, and application to the Pelona Schist, Southern California. J Metamorph Geol 2:13–21

Guiraud M, Powell R (2006) P-V–T relationships and mineral equilibria in inclusions in minerals. Earth Planet Sci Lett 244(3–4):683–694. https://doi.org/10.1016/j.epsl.2006.02.021

Herbosch A, Liegeois J-P, Pin C (2016) Coticules of the Belgian type area (Stavelot-Venn Massif); Limy turbidites within the nascent Rheic oceanic basin. Earth Sci Rev 159:186–214

Hillert M (2008) Phase equilibria, phase diagrams and phase transformations: their thermodynamic basis. Cambridge University Press, Cambridge

Hodges KV, Spear FS (1982) Geothermometry, geobarometry and the Al2SiO5 triple point at Mt. Moosilauke, New Hampshire. Am Min 67:1118–1134

Holland TJB, Powell R (1998) An internally-consistent thermodynamic dataset for phases of petrological interest. J Metamorph Geol 16:309–343

Holland TJB, Powell R (2011) An improved and extended internally consistent thermodynamic dataset for phases of petrological interest, involving a new equations of state for solids. J Metamorph Geol 29:333–383

Kelly ED, Carlson WD, Ketcham RA (2013) Crystallization kinetics during regional metamorphism of porphyroblastic rocks. J Metamorph Geol 31:963–979. https://doi.org/10.1111/jmg.12052

McLean D (1965) The science of metamorphism in metals. In: Pitcher WS, Flinn GW (eds) Controls of metamorphism. Oliver and Boyd, Edinburgh, pp 103–118

Pattison DRM, de Capitani C, Gaidies F (2011) Petrological consequences of variations in metamorphic reaction affinity. J Metamorph Geol 29(9):953–977. https://doi.org/10.1111/j.1525-1314.2011.00950.x

Ridley J, Thompson AB (1986) The role of mineral kinetics in the development of metamorphic microtextures. In: Walther JV, Wood BJ (eds) Fluid-rock interactions during metamorphism. Springer Verlag, New York, pp 80–97

Schmidt A, Pourteau A, Candan O, Oberhansli R (2015) Lu-Hf geochronology on cm-sized garnets using microsampling: New constraints on garnet growth rates and duration of metamorphism during continental collision (Menderes Massif, Turkey). Earth Planet Sci Lett 432:24–35

Spear FS (2017) Garnet growth after overstepping. Chem Geol 466:491–499

Spear FS, Pyle JM (2010) Theoretical modeling of monazite growth in a low-Ca metapelite. Chem Geol 266:218–230

Spear FS, Rumble D III (1986) Pressure, temperature and structural evolution of the Orfordville Belt, west-central New Hampshire. J Petrol 27:1071–1093

Spear FS, Wolfe OM (2019) Implications of overstepping of garnet nucleation for geothermometry, geobarometry and P-T path calculations. Chem Geol. https://doi.org/10.1016/j.chemgeo.2019.119323

Spear FS, Wolfe OM (2020) Revaluation of "equilibrium" P-T paths from zoned garnet in light of quartz inclusion in garnet (QuiG) barometry. Lithos 372:10

Spear FS, Thomas JB, Hallett BW (2014) Overstepping the garnet isograd: a comparison of QuiG barometry and thermodynamic modeling. Contrib Miner Petrol 168(3):1–15. https://doi.org/10.1007/s00410-014-1059-6

Thomas JB, Spear FS (2018) Experimental study of quartz inclusions in garnet at pressures up to 3.0 GPa: evaluating validity of the quartz-in-garnet inclusion elastic thermobarometer. Contrib Mineral Petrol. https://doi.org/10.1007/s00410-018-1469-y

Thomas JB, Watson EB, Spear FS, Shemella PT, Nayak SK, Lanzirotti A (2010) TitaniQ under pressure: the effect of pressure and temperature on Ti-in-quartz solubility. Contrib Miner Petrol 160:743–759

Thompson CV, Spaepen F (1983) Homogeneous crystal nucleation in binary metallic melts. Acta Metall 31:2021–2027

Thomson JA (2001) Relationships of coticule geochemistry to stratigraphy in the Perry Mountain and Megunticook Formations, New England Appalachians. Can Mineral 39:1021–1037

White RW, Powell R, Holland TJB, Johnson TE, Green ECR (2014a) New mineral activity-composition relations for thermodynamic calculations in metapelitic systems. J Metamorph Geol 32(3):261–286. https://doi.org/10.1111/jmg.12071

White RW, Powell R, Johnson TE (2014b) The effect of Mn on mineral stability in metapelites revisited: new a-x relations for manganese-bearing minerals. J Metamorph Geol 32(8):809–828. https://doi.org/10.1111/jmg.12095

Willner AP, Pawlig S, Massone H-J, Herve F (2001) Metamorphic evolution of spessartine quartzites (coticules) in the high-pressure, low-temperature complex at Cahia Mansa, Coastal Cordillera of south-central Chile. Can Mineral 39:1547–1569

Wolfe OM, Spear FS (2018) Determining the amount of overstepping required to nucleate garnet during Barrovian regional metamorphism, Connecticut Valley Synclinorium. J Metamorph Geol 36:79–94

Wolfe OM, Spear FS (2020) Regional quartz inclusion barometry and comparison with conventional thermobarometry and intersecting isopleths from the Connecticut Valley trough, Vermont and Massachusetts, USA. J Petrol 61:1–17